GERLUMPH DATA RELEASE 1: HIGH-RESOLUTION COSMOLOGICAL MICROLENSING MAGNIFICATION MAPS AND eResearch TOOLS

G. Vernardos[1], C. J. Fluke[1], N. F. Bate[2], and D. Croton[1]
[1] Centre for Astrophysics & Supercomputing, Swinburne University of Technology, P.O. Box 218, Hawthorn, Victoria, 3122, Australia
[2] Sydney Institute for Astronomy, School of Physics, A28, University of Sydney, NSW, 2006, Australia

ABSTRACT

As synoptic all-sky surveys begin to discover new multiply lensed quasars, the flow of data will enable statistical cosmological microlensing studies of sufficient size to constrain quasar accretion disk and supermassive black hole properties. In preparation for this new era, we are undertaking the GPU-Enabled, High Resolution cosmological MicroLensing parameter survey (GERLUMPH). We present here the GERLUMPH Data Release 1, which consists of 12,342 high resolution cosmological microlensing magnification maps and provides the first uniform coverage of the convergence, shear, and smooth matter fraction parameter space. We use these maps to perform a comprehensive numerical investigation of the mass-sheet degeneracy, finding excellent agreement with its predictions. We study the effect of smooth matter on microlensing induced magnification fluctuations. In particular, in the minima and saddle-point regions, fluctuations are enhanced only along the critical line, while in the maxima region they are always enhanced for high smooth matter fractions (≈ 0.9). We describe our approach to data management, including the use of an SQL database with a Web interface for data access and online analysis, obviating the need for individuals to download large volumes of data. In combination with existing observational databases and online applications, the GERLUMPH archive represents a fundamental component of a new microlensing eResearch cloud. Our maps and tools are publicly available at http://gerlumph.swin.edu.au/.

Key words: accretion, accretion disks – gravitational lensing: micro – quasars: general

Online-only material: color figures

1. INTRODUCTION

Gravitational lensing studies the effect of matter on the propagation of light through the universe. Observationally, gravitational lensing is characterized by the creation of multiple images or arcs (strong lensing), coherent shape distortions (weak lensing), or high magnifications due to compact objects (microlensing; Schneider et al. 2006). Quasar microlensing, the effect on the magnification of individual images in a multiply imaged quasar due to an ensemble of stellar-mass compact objects near the line of sight, has been well established as a tool for studying the structure of quasars (Schmidt & Wambsganss 2010).

The magnitude of the microlensing effect depends strongly on the size of the emitting source; smaller sources produce more significant microlensing induced magnification variations (Wambsganss et al. 1990). The relevant scale here is the Einstein radius, $R_{\rm Ein}$, the radius of the symmetric ring that occurs when a source is directly aligned with a gravitational lens or microlens:

$$R_{\rm Ein} = \sqrt{\frac{D_{\rm os} D_{\rm ls}}{D_{\rm ol}} \frac{4G\langle M \rangle}{c^2}} \, . \quad (1)$$

This depends on the angular diameter distances from observer to lens, $D_{\rm ol}$, observer to source, $D_{\rm os}$, and lens to source, $D_{\rm ls}$, and the mean mass of the microlenses $\langle M \rangle$. A typical value for $R_{\rm Ein}$ is $5.35 \pm 1.2 \times 10^{16}$ cm, which is the mean of 59 lensed systems from the CASTLES[3] project that have redshifts for both the lens and source available (for $\langle M \rangle = 1\, M_\odot$ and $H_0 = 70$ km s^{-1} Mpc^{-1}).

Since its suggestion by Chang & Refsdal (1979) and subsequent discovery by Irwin et al. (1989), microlensing has been used to study the physical and geometrical properties of quasars, ranging from the broad emission line region (BELR; $\sim 10^{17}$ cm) to the accretion disk ($\sim 10^{15}$ cm) surrounding the central supermassive black hole. For a few systems, the size and temperature profiles of accretion disks have been found to be generally consistent with the Shakura & Sunyaev (1973) thin-disk model (Anguita et al. 2008; Bate et al. 2008; Eigenbrod et al. 2008; Mosquera et al. 2011; Blackburne et al. 2011). However, Floyd et al. (2009) rule out this model for the gravitational lens system SDSSJ0924+0219. Morgan et al. (2010) use microlensing deduced properties of the disk to study the central supermassive black hole for 11 quasars, and although the results agree with a thin disk model, a very low radiative efficiency ($\sim 0.01\%$) is implied. Dai et al. (2010) found that the X-ray emission of RXJ1131−1231 is located in a small region ($\sim 10^{14}$ cm) near the central black hole. Sluse et al. (2012) studied 17 lensed quasars and found that the geometry of the BELR is not necessarily spherically symmetric.

The above studies have focused either on single objects or small samples from the ~ 90 currently known lensed quasars (Mosquera & Kochanek 2011). This is because long-term monitoring and/or multiwavelength observations require a lot of effort and resources, e.g., Poindexter et al. (2008) use data spanning a 13 yr period and 11 bands for the double lens HE1104−1805. However, this is about to change with the new generation of synoptic all-sky survey telescopes, such as the Large Synoptic Survey Telescope (LSST; LSST Science Collaborations et al. 2009), Pan-STARRS (Kaiser et al. 2002), and SkyMapper (Keller et al. 2007), which are expected to survey the entire sky regularly. These facilities are expected to discover a few thousand microlensing candidates

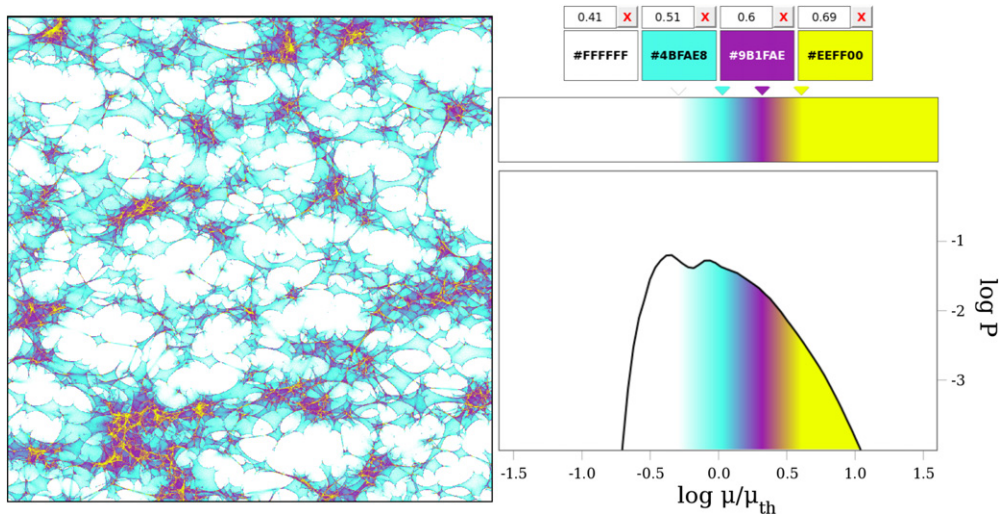---

[3] http://www.cfa.harvard.edu/castles/

Figure 1. Example of the usage of the "Colorbar" tool. The caustic network of a magnification map can be highlighted with different colors at the same time as its corresponding magnification probability distribution. In this example we can see areas of low magnification, or demagnification, ($\mu < 0.3\mu_{\text{th}}$) shown in white, areas of almost no magnification ($\mu \approx \mu_{\text{th}}$) shown in cyan, areas of high magnification ($\mu \approx 3\mu_{\text{th}}$) shown in purple, and finally, areas of very high magnification ($\mu > 3\mu_{\text{th}}$) shown in yellow.

(A color version of this figure is available in the online journal.)

(Oguri & Marshall 2010) and provide regular monitoring without any additional effort. As the number of lensed quasars increases, it becomes ever more important to move from single-object studies to statistically meaningful samples.

On the theoretical side, the basic tool for microlensing studies is the magnification map (hereafter "map"): a statistical representation of the combined effects of an ensemble of microlenses presented as a pixellated image in the source plane (a typical network of caustics, i.e., regions of high magnification in the source plane, can be seen in the example map of Figure 1).

A map is defined in terms of the convergence, κ, which describes the combined focusing power of the compact microlenses, κ_*, and smooth matter, κ_{s}, where $\kappa = \kappa_* + \kappa_{\text{s}}$, and the shear, γ, which describes the distortion applied due to the external mass distribution of the lens galaxy. A further useful parameterization is to define the smooth matter fraction, $s = \kappa_{\text{s}}/\kappa$. Additional parameters required to generate a magnification map, namely, the mass and positions of the microlenses, and the width, resolution, and statistical accuracy of the map, are discussed in Section 2. For studies of specific systems, additional physical parameters may need to be introduced, e.g., motions of the microlenses (Mosquera et al. 2013).

Magnification maps can be used to study the size and geometry of the source by extracting model light curves (the light-curve method, e.g., Morgan et al. 2010), or the temperature profile of the accretion disk by producing probability distributions of the flux in different wavelengths (the snapshot method, e.g., Bate et al. 2008). Producing a magnification map is a computationally demanding task; however, there are a few methods available (Wambsganss 1999; Kochanek 2004; Thompson et al. 2010; Mediavilla et al. 2011), all of which use a variation of the inverse ray-shooting technique (Kayser et al. 1986).

In preparation for the imminent discoveries of new microlensed quasars by the future surveys, a systematic exploration of the microlensing parameter space should be considered (Bate & Fluke 2012, hereafter BF12). In this work, we report on the first results from the GPU-Enabled, High Resolution, cosmological MicroLensing parameter survey (GERLUMPH), using the ~100 teraflop s^{-1} GPU-Supercomputer for Theo-

Table 1
The GERLUMPH Data Sets

Parameters	GD0	GD1
$N_{\kappa,\gamma}$	170	1122
N_{s}	1	11
Width (R_{Ein})	24	25
Resolution (pixels)	4096^2	10000^2
N_{sets}	15	1
Total maps	2550	12342
GPU time (days)	213	2902
data size (TB)	0.16	4.5

Notes. N denotes the number of different values for each parameter, e.g., $N_{\kappa,\gamma}$ is the number of individual κ, γ grid locations, N_{sets} indicates the different sets of random microlens positions, etc. GPU time is the computational time used to generate the maps on a single GPU.

retical Astrophysics Research (gSTAR) and the direct inverse ray-shooting method of Thompson et al. (2010) to address the time-consuming map calculations.

This paper describes the GERLUMPH Data Release 1 (GD1) maps, which comprises a complete set of high resolution maps in the κ, γ, and s parameter space. Moreover, we also release the GERLUMPH Data 0 (GD0) maps, which were used in Vernardos & Fluke (2013, hereafter VF13). The properties of the two data sets are summarized in Table 1 and presented in more detail in Section 2, where we describe our approach to a microlensing parameter survey and compare it to that of BF12. In Section 3, we present the results of two initial applications: an extensive numerical investigation of the mass-sheet degeneracy, and a study of the effect of smooth matter on microlensing-induced magnification fluctuations, throughout the κ, γ, and s parameter space. We make our data publicly available via a web server[4] and provide online tools for map analysis, described in Section 4. Discussions about our results and eResearch approach
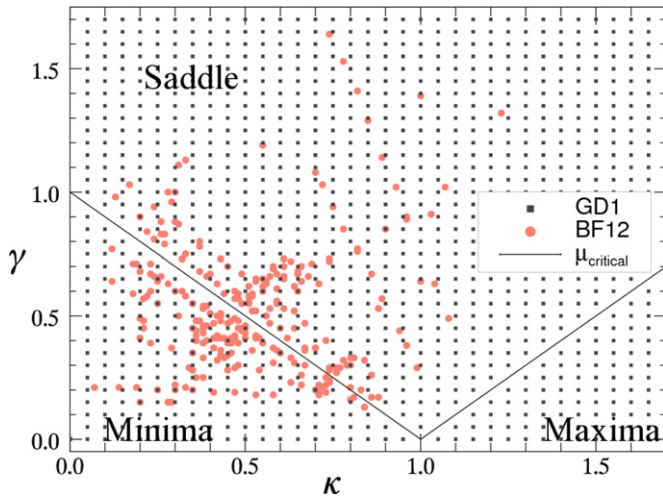

Figure 2. κ, γ values used in GD1 (black squares) and the 266 unique κ, γ pairs from existing macro-models (circles; light red online) as compiled by BF12. GD1 maps cover the range of the existing macro-models; there is always a GD1 map within $\Delta\kappa, \Delta\gamma \leqslant 0.025$ of a model point. The solid line ($\mu_{critical}$) is the critical line, i.e., the locus of $\mu_{th} \to \infty$. An interactive version of this plot and the compilation of BF12 can be found online in the macro-model section of the GERLUMPH server.

(A color version of this figure is available in the online journal.)

follow in Sections 5 and 6. We present our conclusions in Section 7.

2. SURVEY SPECIFICATIONS

We have used our GPU-D ray-shooting code (Thompson et al. 2010; Bate et al. 2010; VF13) in combination with the gSTAR supercomputer facility to generate the GD1 data set of 12,342 magnification maps. The computation of the caustic structure in each map depends on eight parameters, which can be categorized into three groups: macromodel parameters, parameters of the microlenses, and map characteristics. Our choice of parameters for GD1 (and GD0) is shown in Table 1 and discussed below:

2.1. Macromodel (External) Parameters

In order to understand multiply imaged systems, one has to assume a model for the mass distribution of the galaxy lens (e.g., Schneider et al. 2006). These models, hereafter called "macromodels," are chosen on the basis of how well they can reproduce a number of observed properties, e.g., the positions of the multiple (macro) images. The values of κ, γ are extracted from the macromodel at each position on the lens plane and can be used to calculate the magnification of each macroimage,

$$\mu_{th} = \frac{1}{(1-\kappa)^2 - \gamma^2} . \qquad (2)$$

κ, γ can then be used in the following stage of microlensing modeling, i.e., generating magnification maps.

Our maps cover the κ, γ parameter space uniformly: $0.0 < \kappa < 1.7$, $0.0 \leqslant \gamma \leqslant 1.7$, with $\Delta\kappa, \Delta\gamma = 0.05$. Smooth matter is taken into account for each κ, γ combination by generating maps for $0 \leqslant s \leqslant 0.9$, with $\Delta s = 0.1$, and $s = 0.99$. The coverage of the κ, γ parameter space by GD1 is shown in Figure 2, together with existing values for 23 multiply lensed systems, extracted from a number of macromodels from the literature (BF12). The critical line, i.e., where $\mu_{th} \to \infty$, divides the κ, γ parameter space into the minima, saddle-point, and

maxima regions. These regions correspond to the extrema of the time-delay surface, which is where the macroimages form (see Blandford & Narayan 1986, for details).

It is important to point out here that there is a limit to how uniquely determined the macromodel derived κ, γ values can be due to the mass-sheet degeneracy (Falco et al. 1985; Gorenstein et al. 1988). Scaling the mass distribution of the lens and adding a homogeneous surface mass density (mass-sheet) will result in a transformation of coordinates in the source plane, which cannot be directly observed, leaving all other observables unchanged vis-a-vis image positions and shapes, flux ratios, etc. This means that we cannot uniquely determine the lens-galaxy mass distribution, and consequently the resulting κ, γ, without additional information about the source (e.g., absolute size or luminosity) or about the lens-galaxy (e.g., mass derived from observations of stellar dynamics).

2.2. Parameters of the Microlenses

It has been known that the mass of the microlenses has a negligible effect on the magnification probability distribution (MPD) of a magnification map over most of the parameter space (Wambsganss 1992; Lewis & Irwin 1995; Wyithe & Turner 2001; Schechter et al. 2004). Therefore, we adopt the simplest treatment of the microlens mass function vis-a-vis a constant mass of $1\,M_\odot$.

VF13 used GD0 to study systematic map properties for the case of compact matter only ($s = 0$). One of their results concerned the effect of randomly positioning the microlenses on the lens plane. It was found that changing the microlens positions leads to statistically equivalent maps over most of the κ, γ parameter space. However, there are regions of parameter space, i.e., the maxima region and along the critical line for $\kappa \lesssim 1$ (Figure 6, VF13), where one particular set of microlens positions may lead to a quite different MPD (but still an equally valid choice). Therefore, more than one map would be needed in those regions for subsequent calculations to be representative. We have chosen to calculate a single map per κ, γ, s combination, keeping in mind that our results may be affected by this known systematic.

2.3. Map Characteristics

VF13 find that the smaller the width of a map, the more likely it is to get statistically different maps for a given combination of κ, γ (Figure 7, VF13). The GD1 maps have a width of 25 R_{Ein}, which is high enough to minimize this effect while still keeping the necessary computations within our capabilities.

The map resolution is set to 10000^2 pixels. This corresponds to 0.0025 R_{Ein}, or 1.34×10^{15} cm for a typical value of R_{Ein}. These maps are suitable for studying spatial scales from the accretion disk to the BELR for the sample of known multiply imaged quasars (see Section 2.1 of BF12 for a justification of this choice).

Microlensing effectively produces deviations from the macromodel-predicted magnification of a background source, toward high and low magnifications (Paczynski 1986). Both cases are of interest, the former for studying caustic crossing events (e.g., Witt et al. 1993; Anguita et al. 2008) and the latter in the case of anomalous flux systems (e.g., Schechter et al. 2004; Bate et al. 2008). The inverse ray-shooting technique measures the magnification by shooting a large number of rays through the lens plane and mapping them on the source plane. Low magnification means that a small number of rays reached
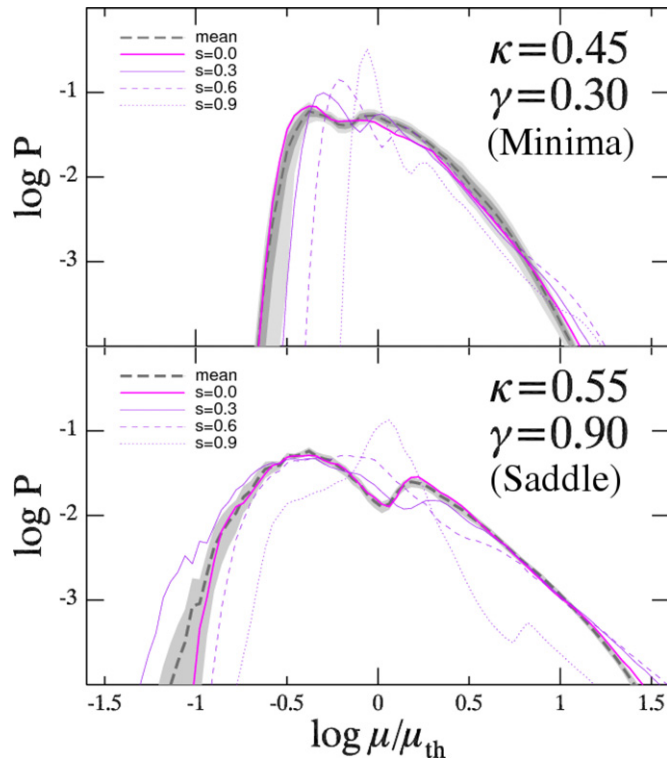
Figure 3. Magnification probability distribution (MPD) of a GD1 10000^2 pixel map (thick solid line; magenta in the online journal), compared to the mean MPD obtained by VF13 (thick dashed line), for κ, γ, s equal to (0.45, 0.3, 0), top panel, and (0.55, 0.9, 0), bottom panel. The gray area is one standard deviation from the mean MPD. The thin solid, dashed, and dotted lines (purple in the online journal) are the MPDs for s equal to 0.3, 0.6, and 0.9, respectively. This figure can be reproduced for any value of κ, γ via the tools section of the GERLUMPH server.

(A color version of this figure is available in the online journal.)

Figure 4. Probability surfaces (shades of red in the online journal) with respect to the magnification and s. The magnification range is the same as in Figure 3. Contours are drawn at $\log P = (-1.25, -1.5, -1.9, -2.3, -3)$ to better depict the shape of the surfaces. The high resolution MPDs of Figure 3 can be seen here for the corresponding values of s (horizontal dotted lines). The vertical dashed lines indicate $\mu = 0.3\mu_{th}$ and $\mu = 3\mu_{th}$. This figure can be reproduced for any value of κ, γ via the tools section of the GERLUMPH server.

(A color version of this figure is available in the online journal.)

the examined position in the source plane. Therefore, for a map to accurately probe the ranges of magnification of interest, we need to shoot a very large number of rays, $\mathcal{O}(10^{10})$. The final average number of rays per map pixel, N_{avg}, among the GD1 maps is 457 ± 26, which is high enough (the systematics of N_{avg} have been examined by VF13, who found an average of 302 ± 24 rays per pixel to be sufficient).

2.4. GD1 Data

The total data size for GD1 is 4.5 TB. Maps are stored in binary format, using unsigned integers to represent the number of rays per pixel, leading to a file size of 381 MB per map. BF12 report smaller file sizes and suggest using an unsigned short integer data type. In our case, however, we have ray counts that exceed 65,536, the maximum number for unsigned short integer representation, due to the much larger total number of rays that we are shooting. gSTAR has ∼1.7PB of storage space, therefore storing a few tens of thousands of high resolution maps is not a problem. Our Web server configuration as well as how to access and download the GD1 maps are described in Section 4.

File size may become important for users downloading tens or hundreds of maps from the GERLUMPH Web server. Longer term, our preferred model of operation for parameter-space investigations is fully remote analysis via online e-tools, obviating the need for individuals to download large volumes of data. For now, we use standard Unix compression tools (`bzip2`)
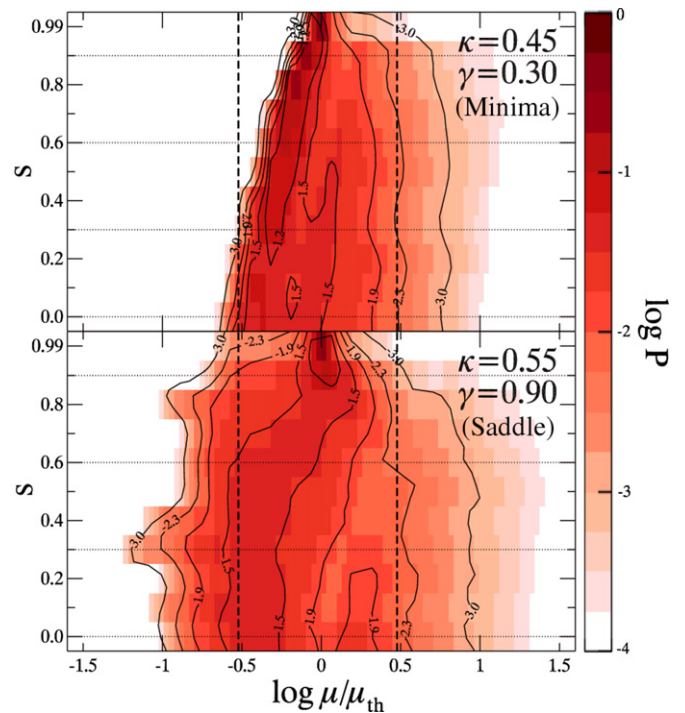
to compress the binary files delivered to the users over the internet, reducing file sizes by ≈65%.

3. RESULTS

We begin by examining the agreement between the MPDs of the GD1 maps and the mean MPD determined by VF13 from 15 different maps at lower resolution (4096^2 pixels) in the case without smooth matter. As an example, in Figure 3 we compare the mean MPD, thick dashed line, and the MPD of GD1, thick solid line, for two trial combinations, $\kappa, \gamma = (0.45, 0.3)$, corresponding to the minima region, and $\kappa, \gamma = (0.55, 0.9)$, corresponding to the saddle-point region. Apart from very low magnifications ($\mu < 0.1\mu_{th}$), the high resolution MPD agrees well with the lower resolution mean MPD. The behavior for low μ is expected due to the low ray counts (small number statistics), however, the higher resolution MPD is still within one standard deviation of the mean.

In Figure 3, we also show for comparison the MPDs for three different smooth matter fractions, $s = 0.3, 0.6, 0.9$. It is expected that as the smooth matter fraction is varied, the shape of the MPD changes (more smooth matter means less microlenses). In Figure 4 we show the probability surface as a function of the magnification and smooth matter fraction. This representation highlights the changing width of the MPD and the appearance of additional higher-probability peaks in the MPDs occurring between $0.3 \simeq \mu/\mu_{th} \simeq 3.0$. These additional peaks are related to the number of extra microimage pairs, which increase near the critical line (Granot et al. 2003). We stress here that our online tools (Section 4) make these comparisons straightforward for any point in parameter space.
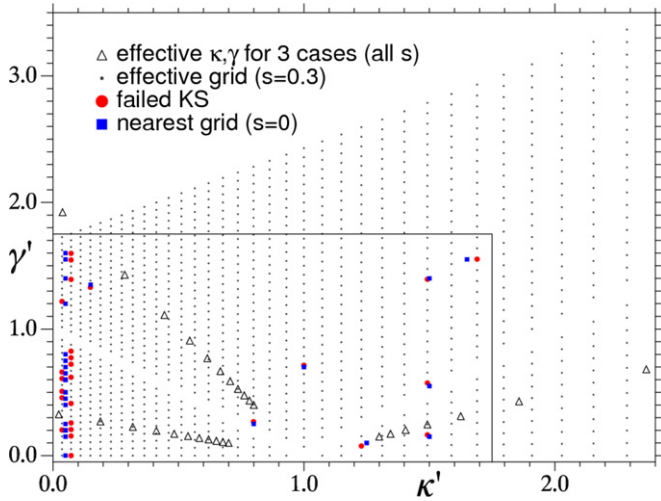
Figure 5. Effective κ', γ' parameter space. For three combinations of $\kappa, \gamma = (0.7, 0.1), (0.8, 0.4), (1.3, 0.15)$, open triangles show the equivalent κ', γ' for all values of s (within the plot range) that we have used. The dots correspond to the effective grid of the subset of GD1 maps with $s = 0.3$. Filled circles (red in the online journal) indicate the cases that failed the KS test with their nearest $s = 0$ grid point, shown as a filled square (blue in the online journal). The rectangular region corresponds to the range shown in Figure 2.

(A color version of this figure is available in the online journal.)

3.1. Mass-sheet Degeneracy

While we have chosen to perform a parameter survey by uniformly varying κ, γ, and s (Figure 2), this is not the only possible sampling strategy. The mass-sheet degeneracy is a transformation between equivalent lens models that produce the same observables (see Section 2.1). In our case, the three-dimensional parameter space, $\kappa - \gamma - s$, transforms into the two-dimensional effective parameter space, $\kappa' - \gamma'$, through:

$$\kappa' = \frac{(1-s)\kappa}{1-s\kappa}, \quad \gamma' = \frac{\gamma}{1-s\kappa} \quad (3)$$

In Figure 5, we show the κ', γ' locations for all the GD1 maps with $s = 0.3$ (black dots). The rectangular area of Figure 5 corresponds to the κ, γ range shown in Figure 2, our original κ, γ grid of 1122 points, and encloses 728 of the κ', γ' pairs of the $s = 0.3$ subset. It can be seen from this example that the relevant GD1 maps do not cover the effective parameter space uniformly, i.e., more densely for $\kappa' < 1$ (minima region) and more sparsely for $\kappa' > 1$.

To further illustrate the relationship between the GD1 maps and the effective parameter space, we present three κ, γ combinations: $(0.7, 0.1), (0.8, 0.4)$ and $(1.3, 0.15)$, one from each of the minima, saddle-point, and maxima regions of parameter space. For each case we calculate κ', γ', shown in Figure 5 as open triangles, for all available steps in the smooth matter fraction. As the smooth matter content is increased, the equivalent κ', γ' pairs move outward radially from $\kappa', \gamma' = (1, 0)$, as expected; that is the reason why for $\kappa, \gamma = (1.3, 0.15)$ maps with $s > 0.7$ lie outside the range of the plot.

The mass-sheet degeneracy suggests that a given GD1 map should give the same microlensing outcomes as the effective-space map. While the number of microlenses will be almost equal, the actual caustic networks on the equivalent maps will be different because we have used random microlens positions for all our maps. However, their corresponding MPDs should be statistically equivalent. Moreover, since a given κ', γ' will
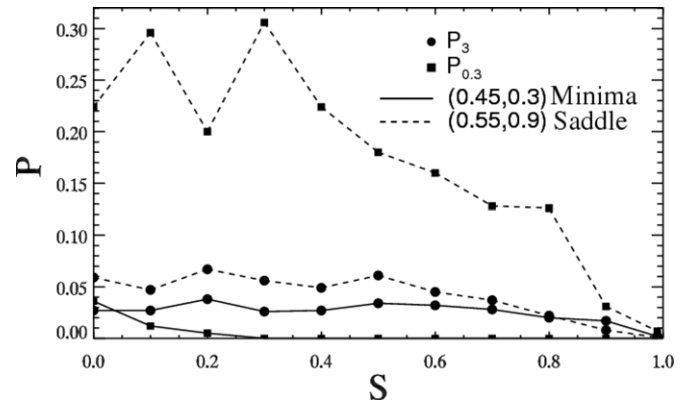

Figure 6. Value of P_3 (circles) and $P_{0.3}$ (squares) as a function of s, for κ, γ equal to $(0.45, 0.3)$ (dashed line) and $(0.55, 0.9)$ (solid line). This figure can be reproduced for any value of κ, γ via the tools section of the GERLUMPH server.

Table 2
KS Test Results for All Values of s

s	N_{total}	N_{failed}	$N_{\text{total}}^{\kappa \geqslant 0.05}$	$N_{\text{failed}}^{\kappa \geqslant 0.05}$	% Failed for $\kappa \geqslant 0.05$
0.1	953	37	920	36	3.9
0.2	822	24	789	22	2.8
0.3	728	26	695	20	2.9
0.4	633	27	600	18	3.0
0.5	562	26	529	11	2.0
0.6	438	27	420	6	1.4
0.7	436	42	373	10	2.7
0.8	423	60	269	4	1.5
0.9	348	103	180	4	2.2
0.99	317	276	10	0	0.0

Notes. Number of total, N_{total}, and failed, N_{failed}, cases for the full effective grid, as well as for the grid with $\kappa \geqslant 0.05$, for all values of the smooth matter fraction s. The failed cases for $\kappa \geqslant 0.05$ are also shown as a percentage over the total in the last column.

not necessarily coincide with our original grid, we make our comparisons with the nearest grid point.

To examine the equivalence of the full parameter space with the effective space, we performed a Kolmogorov–Smirnov (KS) test between each of the 728 κ', γ' maps with $s = 0.3$ and the nearest $\kappa, \gamma, s = 0$ map from GD1. The null hypothesis was that the MPDs are the same. Only 26 nearest neighbor pairs had a p-value less than 0.05, meaning that they failed the test, and they are shown as filled circles in Figure 5. The positions of the $s = 0$ GD1 maps with which these cases were compared are shown as filled squares. It can be seen that the effective grid points lie quite far from our grid points with $\kappa = 0.05$, leading to a clustering of cases that failed the KS test for $\kappa < 0.1$. This can be true for a few of the other failed cases as well; however, we point out that the latter ones fall in regions of parameter space where random microlens position systematics may play a role (see VF13, Figure 6(a)).

We have performed a similar analysis for the remaining values of the smooth matter fraction in GD1. We expect more effective grid points to appear for very low values of κ' as the smooth matter fraction is increased, e.g., open triangles in the minima region of Figure 5. The nearest original grid points to those cases will have $\kappa = 0.05$, the lowest value in GD1, which may be too far away to have a similar MPD and consequently fail the KS test. This can be seen in the first three columns of Table 2, which show the total number of effective grid points lying inside our
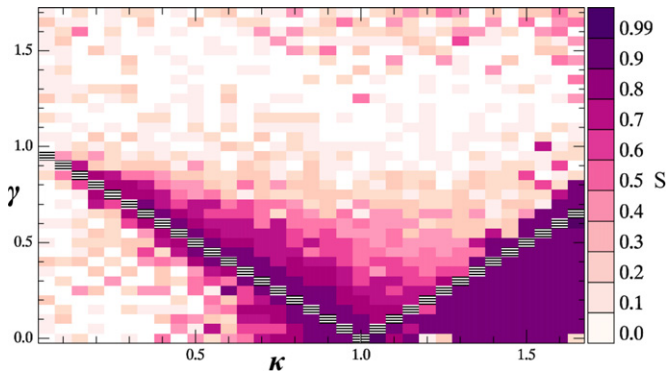
Figure 7. Value of *s* for which the maximum probability for magnifications higher than $3\mu_{th}$ occurs, shown across the parameter space. The presence of smooth matter enhances the high magnification fluctuations in the maxima region and the region along the critical line. For $s = 0.99$, the probability drops, thus setting an upper limit to this enhancement.

(A color version of this figure is available in the online journal.)

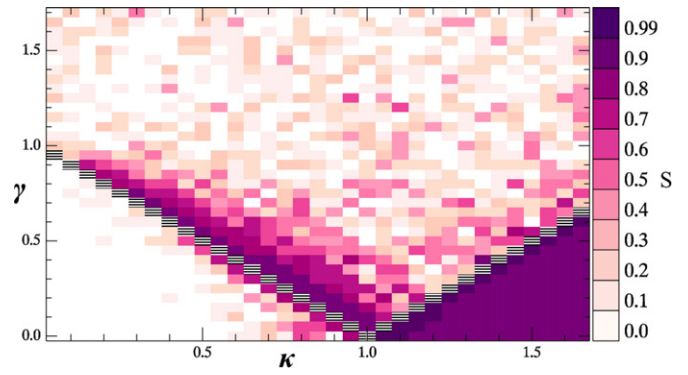**Figure 8.** Value of *s* for which the maximum probability for magnifications lower than $0.3\mu_{th}$ occurs, shown across the parameter space. The presence of smooth matter enhances the high demagnification fluctuations in the maxima region and the region just above the critical line for $\kappa < 1$.

(A color version of this figure is available in the online journal.)

original grid and the number of cases that failed the KS test, as *s* is increased. For very high *s*, the majority of effective grid points lie below $\kappa = 0.05$ and so have a statistically different MPDs, e.g., for $s = 0.99$ all the failed cases lie below $\kappa = 0.05$, where 97% of the total effective grid points are also located. However, if we take into account only the effective grid points with $\kappa \geqslant 0.05$, the number of cases that failed the KS test lies between 0% and 4% (last three columns of Table 2). These cases can be effected by random microlens position systematics, or it could also be that the nearest grid point lies too far away to have a similar MPD.

The above experiments show that the MPDs are similar throughout the examined parameter space, and are in agreement with what is expected from the mass-sheet degeneracy.

3.2. Magnification Fluctuations

As introduced in Section 2.3, microlensing induced variations toward high and low magnifications are expected to affect different kinds of observations. High magnification events (e.g., Anguita et al. 2008) are effected by the high magnification tail of the MPDs, while anomalous flux systems more likely occur as a result of the demagnification of one of the images due to a combination of both smooth matter and compact objects (Schechter & Wambsganss 2002). In order to investigate how smooth matter effects the high magnification part of the MPDs, we define a quantity, P_3, that has been used in the past (Rauch et al. 1992; Wambsganss 1992) to measure the total probability in the magnification range $3\mu_{th} < \mu < +\infty$ (right of the dashed line in Figure 4):

$$P_3 = \int_3^{+\infty} P(\mu/\mu_{th}) d(\mu/\mu_{th}) = \sum^{\mu_i > 3\mu_{th}} P(\mu_i), \qquad (4)$$

A similar quantity is defined for demagnifications:

$$P_{0.3} = \int_{-\infty}^{0.3} P(\mu/\mu_{th}) d(\mu/\mu_{th}) = \sum^{\mu_i < 0.3\mu_{th}} P(\mu_i), \qquad (5)$$

which is the total probability in the magnification range $-\infty < \mu < 0.3\mu_{th}$ (left of the dashed line in Figure 4). We examine the effect of smooth matter on these two quantities throughout the original κ, γ, *s* parameter space.

Figure 6 shows the variation of P_3 (filled circles) and $P_{0.3}$ (filled squares) as *s* is increased, for two trial combinations $\kappa, \gamma = (0.45, 0.3)$ (solid lines) and $\kappa, \gamma = (0.55, 0.9)$ (dashed lines). The situation is quite different between the minima and saddle-point regions of parameter space. It is clear that the saddle-point case is much more demagnified than the minima one. Moreover, increasing the presence of smooth matter past $s = 0.2$ suppresses demagnifications in the minima region. High magnifications for the saddle-point case are two times more likely than the minima case. Both high and low magnifications start to decrease past roughly $s = 0.5$ for the saddle-point case, while the decrease is slower and starts around $s = 0.6$ for high magnifications for the minima.

By performing a similar analysis in other κ, γ locations, we can identify the general trend of P_3 and $P_{0.3}$ with respect to *s* across parameter space regions. In the minima and saddle-point regions, there is a value of *s* which gives the maximum probability for high/low magnifications. This can be seen in Figures 7 and 8, where we show the value of *s* for which the maximum P_3 and $P_{0.3}$ occur, for a given κ, γ combination. The maximum never occurs at $s = 0.99$ because there are almost no compact objects, which confirms our expectation that there is a limit to the enhancement of microlensing-induced fluctuations due to smooth matter (Schechter & Wambsganss 2002).

The maxima region is different than the minima and saddle regions, since the maximum P_3 and $P_{0.3}$ occur consistently at $s = 0.9$ throughout it. With closer examination, there are high oscillations for low values of *s*, which shift the maximum of P_3 to lower *s* in three cases: $\kappa = (1.2, 1.25, 1.65)$ and $\gamma = 0.0$, but the overall behavior does not change. By identifying the particular behavior of the maxima region from Figures 7 and 8, we can now go back and examine the MPDs in detail for an example case. In Figure 9, we show the MPDs for four different smooth matter fractions, $s = 0.0, 0.3, 0.6, 0.9$, for a trial combination of $\kappa, \gamma = (1.45, 0.1)$ in the maxima region (the mean MPD from VF13 for $s = 0$ is also shown). The MPD for $s = 0.9$ (dotted line) is the one that suppresses magnifications between $0.3 < \mu/\mu_{th} < 3.0$ and provides the most enhanced fluctuations from μ_{th}.

4. THE WEB SERVER AND ONLINE TOOLS

To support online access to the GERLUMPH maps, we have developed a series of tools that can be used in a Web browser with JavaScript support enabled. The GERLUMPH server is based on
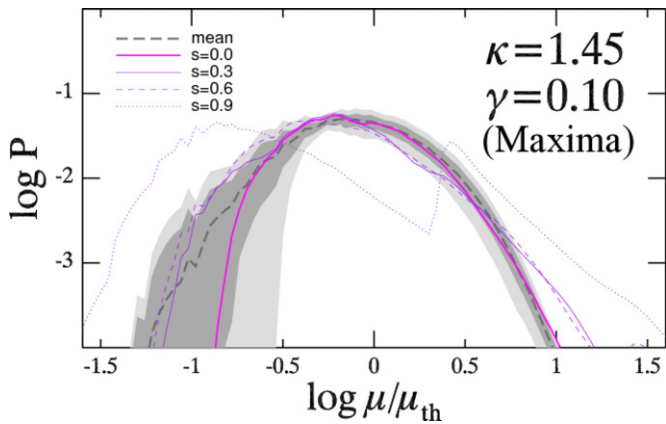
Figure 9. Example magnification probability distribution (MPD) from the maxima region, for $\kappa, \gamma = (1.45, 0.1)$ (similar to Figure 3). The thin solid, dashed, and dotted lines (purple online) are the MPDs for s equal to 0.3, 0.6, and 0.9, respectively. The probability for very high magnifications and demagnifications is maximized for $s = 0.9$. The mean MPD for $s = 0$, thick dashed line, and the one standard deviation region, gray area, from VF13 are also shown for comparison.

(A color version of this figure is available in the online journal.)

the open-source LAMP software bundle (Linux/GNU Apache MySQL PHP; Lee & Ware 2002). For specific applications we find that WebGL[5] provides a performance boost, especially for online image processing. In the following, we outline the data and services provided by the server. A more detailed guide with examples of how to use the GERLUMPH resource can be found online.[6]

The GERLUMPH maps can be retrieved either by a direct query to the map database[7] or by selecting a specific system and a corresponding macro-model.[8] A user can then proceed with downloading the maps, or use one of the provided tools to inspect the map properties.

Currently, we provide online tools to generate graphs similar to Figures 3, 4 and 6, but for any combination of κ, γ, from GD1. There are also tools for reproducing the GD0 data visualizations presented in VF13. Finally, we introduce the "Colorbar," a tool that color-highlights caustics of different magnification on a map, together with the corresponding part of the MPD. An example of the use of "Colorbar" can be seen in Figure 1. All the above tools, together with detailed descriptions and examples, can be accessed in the results section of the GERLUMPH Web site.[9]

We envisage several modes of operation:

1. Particular microlensed systems of interest can be studied by accessing individual parameter-space values, typically through the macro-model tool.
2. For use in external, pre-existing analysis tools or to compare magnification maps or MPDs produced by other means, a small subset of maps would be selected for downloading.
3. For specific parameter-space explorations requiring from 100s to 1000s of GD1 maps, new e-tools should be implemented and made accessible through the Web service. This preferred paradigm of pushing the computation to the

---

[5] Web Graphics Library is a JavaScript API for rendering interactive 3D and 2D graphics within any compatible Web browser, allowing for GPU acceleration.
[6] http://gerlumph.swin.edu.au/guide/
[7] http://gerlumph.swin.edu.au/parsquery/
[8] http://gerlumph.swin.edu.au/macro-models/
[9] http://gerlumph.swin.edu.au/#tools

data (Szalay & Gray 2001; Gray & Szalay 2004) obviates the need for individuals to download (potentially) terabytes of data for local analysis.

5. DISCUSSION

We have presented a first application of the GD1 results: a detailed numerical investigation of the mass-sheet degeneracy. Using the transformations to effective convergence and shear (3), we have compared maps with a variety of smooth matter values to those with $s = 0$, over a region of parameter space relevant to microlensing research ($0.0 < \kappa, \gamma < 1.7$, Figure 5). Fewer than 4% of cases failed the KS test for any value of s available in the GD1 maps (Table 2). The reasons why these cases fail the KS test are well understood: either the nearest original GD1 parameter point was too far from the effective one and thus had a significantly different MPD, or the maps were in a region of parameter space where microlens position systematics should have been taken into account (VF13).

The transition in the MPD shapes in Section 3 (Figures 3 and 4) can be understood in terms of the analytic result of Granot et al. (2003), who attribute the appearance of each peak to the presence of an extra pair of microimages. Increasing s causes the MPDs to become narrower and reduces the probability for extra microimage pairs. While Granot et al. (2003) compared their analytic result only to three cases due to computational limitations, GERLUMPH has enabled such tests anywhere in parameter space. For the moment, such a test cannot be performed online, but users are welcome to download any map and use it with their own tools.

Another application of GD1 is exploring the effect of smooth matter on the high magnification and demagnification parts of the MPDs in the κ, γ parameter space. Including smooth matter increases the total probability of high magnification along the critical line and for increasing κ (Figure 7). In the rest of the parameter space, away from the critical line and the maxima region, the probability of high magnifications is decreased. For demagnifications, the minima, saddle-point, and maxima regions show distinct properties. Smooth matter has almost no effect in the minima region, while just above the critical line, in the saddle-point region, high values of smooth matter ($s = 0.7$–0.9) enhance the low magnification part of the MPD. This effect is slowly reduced as we get further from the critical line. Finally, $s = 0.9$ provides the maximum demagnification probability throughout the maxima region.

Our experiments in Section 3.2 allow us to confirm the findings of Schechter & Wambsganss (2002), who considered the close pair of images of the lensed quasar MG0414+0534, with $\kappa, \gamma = (0.475, 0.425)$ (minimum) and $\kappa, \gamma = (0.525, 0.575)$ (saddle), and found an enhancement in demagnification when including smooth matter. However, our results extend this picture to the entire parameter space, indicating that this only happens close to the critical line, and not in the rest of the minima or saddle-point regions.

Vernardos & Fluke (2013) found that there are specific areas of parameter space where the MPD is effected by the size of the map, and more than one map, or a wider map, would be needed to get a representative behavior. Our present results (Figures 7 and 8) appear consistent throughout these areas, meaning that the uncertainty in the low magnifications does not play an important role in the properties that we are examining.

Finally, we find that the strongest microlensing induced fluctuations consistently occur throughout the maxima region for $s = 90\%$. This result, together with the results of VF13,

indicates that different microlensing signatures should be expected in the maxima region of parameter space. However, maxima images of background quasars are expected to occur near the central regions of the galaxy lens, where the smooth matter fraction should be quite low.

6. FUTURE: eResearch AND THE MICROLENSING CLOUD

As the volume of astronomical data continues to increase, there is a growing need to move more analysis tasks to a remote service model on cloud-like architectures (e.g., Berriman & Groom 2011). This approach of pushing the research question to the data, rather than the traditional method of bringing the data to the desktop, sits at the core of the Virtual Observatory (VO) philosophy (Szalay & Gray 2001; Gray & Szalay 2004).

While most observational data sets are now routinely published in VO-compliant online archives, VO theory is lagging behind (see Teuben et al. 2002, for an early discussion). In part, this is because it has proven complex to define an appropriate data standard, and so each field has focused on its own needs and implementations, such as astrophysical computational simulations (Cassisi et al. 2008; Lemson et al. 2009).

With GD1, we provide an in-progress case study on how to manage a growing online data archive, where the preferred analysis method is to use in-browser tools. As we continue to generate and add additional maps to the GERLUMPH archive, we anticipate that the final data set will comprise ∼60,000 high resolution maps, corresponding to ∼20 TB of data. The number of maps and the amount of data are not too large to be reprocessed, but not small enough that they can be easily downloaded and used by individuals. Indeed, it would be very time and resource consuming to download all, or even significant subsets of these maps, in order to perform parameter space studies of cosmological microlensing.

We are continuing to investigate ways to implement and provide additional tools for online processing, including supporting map and source profile convolutions, automated and interactive extraction of light curves, and an external map upload facility to facilitate model- and technique-based comparisons.

In combination with observational databases (e.g., CASTLES[10] or The Master Lens database[11]) and other online applications (e.g., Mowgli; Naudus et al. 2010), GERLUMPH will become a major piece of a new microlensing eResearch cloud, effectively redesigning the way we approach the analysis and investigation of quasar accretion disks and supermassive black holes in the synoptic survey era.

7. CONCLUSIONS

As new synoptic all-sky surveys commence, the number of known gravitationally lensed quasars is set to increase by a factor of 10, from around 100 (Mosquera & Kochanek 2011) to, potentially, a few thousand (Oguri & Marshall 2010). These discoveries will enable improved understanding of the role that quasars and their central supermassive black holes play in the formation and evolution of galaxies and the large scale structure of the universe. Obtaining the best lensing-based constraints on quasar/black hole properties requires extensive computational modeling, through the generation of microlensing magnification maps. There is a need now to fully explore the connection

between inferred quasar model constraints (such as the size of emission regions, or the accretion disk temperature profile) and the underlying microlensing model.

GERLUMPH is a cosmological microlensing theoretical parameter survey that takes up the challenge of parameter space exploration. GERLUMPH magnification maps can be used with standard analysis techniques (e.g., convolution with source profiles and/or light curve extraction) for applications to observations. However, it is not our intention that GERLUMPH should remove the need for individuals to produce their own magnification maps: indeed such computations and comparisons to GERLUMPH data sets would be encouraged. What makes GERLUMPH unique is the ability to carry out studies systematically across the microlensing parameter space, using a set of online e-tools. This toolbox can be enriched at any time by implementing additional analysis or visualization strategies that the microlensing community may suggest.

We have used the 12,342 maps of GD1 to test the mass-sheet degeneracy, and our results are in agreement with its predictions. We have explored the effect of smooth matter on high magnifications ($>3\mu_{\rm th}$) and demagnifications ($<0.3\mu_{\rm th}$), and found that the presence of smooth matter enhances high magnifications along the critical line and in the maxima region, while demagnifications are enhanced mostly in the saddle-point and maxima regions. Our GD1 data (together with the GD0 data set used in VF13) are publicly available and can be downloaded through our Web server, which also provides an initial set of online analysis tools.

We have gained new insight into the management of moderate-sized (∼20 TB) theory-based astronomy data sets, which will be of benefit to future eResearch projects in astronomy and other sciences. The GERLUMPH data resource aims to provide a computationally demanding piece of the Web-based microlensing computing cloud, and enables a new approach for generating high quality results to interpret upcoming new discoveries of gravitationally lensed quasars.

---

[10] http://www.cfa.harvard.edu/castles/
[11] http://masterlens.astro.utah.edu/

REFERENCES

Anguita, T., Schmidt, R. W., Turner, E. L., et al. 2008, A&A, 480, 327
Bate, N. F., Floyd, D. J. E., Webster, R. L., & Wyithe, J. S. B. 2008, MNRAS, 391, 1955
Bate, N. F., & Fluke, C. J. 2012, ApJ, 744, 90
Bate, N. F., Fluke, C. J., Barsdell, B. R., Garsden, H., & Lewis, G. F. 2010, NewA, 15, 726
Berriman, G. B., & Groom, S. L. 2011, arXiv:1111.0075
Blackburne, J. A., Pooley, D., Rappaport, S., & Schechter, P. L. 2011, ApJ, 729, 34
Blandford, R., & Narayan, R. 1986, ApJ, 310, 568
Cassisi, S., Cervino, M., Lemson, G., et al. 2008, EuroVO-DCA, RI031675, Final report
Chang, K., & Refsdal, S. 1979, Natur, 282, 561
Dai, X., Kochanek, C. S., Chartas, G., et al. 2010, ApJ, 709, 278
Eigenbrod, A., Courbin, F., Meylan, G., et al. 2008, A&A, 490, 933
Falco, E. E., Gorenstein, V. M., & Shapiro, I. I. 1985, ApJL, 289, L1
Floyd, D. J. E., Bate, N. F., & Webster, R. L. 2009, MNRAS, 398, 233
Gorenstein, V. M., Falco, E. E., & Shapiro, I. I. 1988, ApJ, 327, 693
Granot, J., Schechter, P. L., & Wambsganss, J. 2003, ApJ, 583, 575

Gray, J., & Szalay, A. 2004, Commun. ACM, 45, 50
Irwin, M. J., Webster, R. L., Hewett, P. C., Corrigan, R. T., & Jedrzejewski, R. I. 1989, AJ, 98, 1989
Kaiser, N., Aussel, H., Burke, B., et al. 2002, Proc. SPIE, 4836, 154
Kayser, R., Refsdal, S., & Stabell, R. 1986, A&A, 166, 36
Keller, S. C., Schmidt, B. P., Bessell, M. S., et al. 2007, PASA, 24, 1
Kochanek, C. S. 2004, ApJ, 605, 58
Lee, J., & Ware, B. 2002, Open Source Web Development with LAMP: Using Linux, Apache, MySQL, Perl, and PHP (Boston, MA: Addison-Wesley Professional), 496
Lemson, G., & Zuther, J. 2009, Memorie della Societa Astronomica Italiana, 80, 342
Lewis, G., & Irwin, M. 1995, MNRAS, 276, 103
LSST Science Collaborations, et al. 2009, arXiv:0912.0201
Mediavilla, E., Mediavilla, T., Muñoz, J. A., et al. 2011, ApJ, 741, 42
Morgan, C. W., Kochanek, C. S., Morgan, N. D., & Falco, E. E. 2010, ApJ, 712, 1129
Mosquera, A. M., & Kochanek, C. S. 2011, ApJ, 738, 96
Mosquera, A. M., Kochanek, C. S., Chen, B., et al. 2013, ApJ, 769, 53
Mosquera, A. M., Muñoz, J. A., Mediavilla, E., & Kochanek, C. S. 2011, ApJ, 728, 145
Naudus, P., Wallin, J., & Marshall, P. 2010, BAAS, 42, 383
Oguri, M., & Marshall, P. J. 2010, MNRAS, 405, 2579
Paczynski, B. 1986, ApJ, 301, 503

Poindexter, S., Morgan, N., & Kochanek, C. S. 2008, ApJ, 673, 34
Rauch, K. P., Mao, S., Wambsganss, J., & Paczynski, B. 1992, ApJ, 386, 30
Schechter, P. L., & Wambsganss, J. 2002, ApJ, 580, 685
Schechter, P. L., Wambsganss, J., & Lewis, G. F. 2004, ApJ, 613, 77
Schmidt, R. W., & Wambsganss, J. 2010, GReGr, 42, 2127
Schneider, P., Kochanek, C. S., & Wambsganss, J. 2006, in Gravitational Lensing: Strong, Weak, Micro, ed. G. Meylan, P. Jetzer, & P. North (saas-fee a ed.; Berlin: Springer)
Shakura, N., & Sunyaev, R. 1973, A&A, 24, 337
Sluse, D., Hutsemékers, D., Courbin, F., Meylan, G., & Wambsganss, J. 2012, A&A, 544, A62
Szalay, A., & Gray, J. 2001, Sci, 293, 2037
Teuben, P., DeYoung, D., Hut, P., et al. 2002, in ASP Conf. Ser. 281, Astronomical Data Analysis Software and Systems XI, ed. D. A. Bohlender, D. Durand, & T. H. Handley (San Francisco, CA: ASP), 7
Thompson, A. C., Fluke, C. J., Barnes, D. G., & Barsdell, B. R. 2010, NewA, 15, 16
Vernardos, G., & Fluke, C. J. 2013, MNRAS, 434, 832
Wambsganss, J. 1992, ApJ, 386, 19
Wambsganss, J. 1999, JCoAM, 109, 353
Wambsganss, J., Paczynski, B., & Schneider, P. 1990, ApJL, 358, L33
Witt, H., Kayser, R., & Refsdal, S. 1993, A&A, 268, 501
Wyithe, J. S. B., & Turner, E. L. 2001, MNRAS, 320, 21